Dalton Transactions

Accepted Manuscript

ROYAL SOCIETY OF CHEMISTRY

www.rsc.org/dalton

Dalton Transactions

RSCPublishing

ARTICLE

Synchrotron applications to f-element research in the nuclear fuel cycle

Cite this: DOI: 10.1039/x0xx00000x

Melissa A. Denecke[a]

Received 00th January 2012,
Accepted 00th January 2012

DOI: 10.1039/x0xx00000x

www.rsc.org/

Synchrotron-based techniques are increasingly used to characterize radioactive materials and elucidate determinant processes relevant to the nuclear fuel cycle. Many recent advances are driven by the need to characterize such materials with high resolution, for example spatial resolution for studies of localized components of heterogeneous systems and energy resolution for characterising 5f-element oxidation state. Examples of synchrotron-based investigations into f-element chemistry are presented, which illustrate utilizing such high resolution, while pointing out various aspects of synchrotron R&D related to the nuclear fuel cycle. Specifically an example related to separations chemistry performance, an example elucidating immobilisation processes in bedrock, and high energy X-ray emission spectral fingerprint for hexavalent uranium are summarised. Synchrotron-based tools are driving insight into f-element chemistry and geochemistry and are providing data for benchmarking theoretical calculations; the future looks bright.

Introduction

X-ray spectroscopic and scattering techniques using synchrotron radiation are extremely useful to characterize molecular, chemical and physical form of f-elements, in general, and f-elements important to the nuclear fuel cycle in particular. With the increasing availability of experimental stations dedicated to investigations of radioactive material, such techniques increasingly used for studies of 5f elements[1]. Most recently, studies of 5f elements using high energy resolution spectroscopic methods is providing benchmark data, which is driving theoretical developments. By providing direct measures of occupancies and energies of frontier electrons, direct improvements in quantum chemical descriptions of the heavy, relativistic actinide elements are possible and help increase reliability in predictions of their behaviour. This can potentially impact areas of nuclear energy research and development (R&D), as the 5f elements, being the long-lived, alpha-emitting components of nuclear fuel and spent fuel, are of central importance for developing or improving both fuels, separations schemes of spent fuels and waste streams, and evaluation of the radiological safety of proposed strategies for nuclear waste disposal and mitigation of nuclear legacies. The penetration capability of the X-rays used in synchrotron techniques, combined with increasing brilliance delivered by machines and advances in focusing methods, makes it possible to study heterogeneous systems safely in a radiological containment. Illustrative examples demonstrating the advantages of using synchrotron radiation for X-ray Absorption Spectroscopy (XAS) applied to f-elements, of application of focussed X-ray beams for three-dimensional imaging of elemental distributions in heterogeneous, natural samples, and investigation f-element oxidation state/electronic structure using high energy resolution are summarised. Two examples also are directly related to R&D of the nuclear fuel cycle: 1) partitioning of long-lived nuclides from the associated waste stream in reprocessing/recycling of spent nuclear fuel and 2) retention capability of deep geological nuclear waste repository host rock in a worst case scenario of ground water intrusion, where radionuclides can be potentially released.

Application Examples

Partitioning of long-lived actinides from lanthanide fission products

A key challenge facing humanity is to secure a sufficient global supply of energy without increasing emissions harmful to the climate and environment. Without low carbon nuclear power generation in the energy mix, meeting both projected global needs for electricity and the European Commission targets for decarbonisation of energy will not be met[2]. The sustainability of modes of power generation, including nuclear, depends on further development of future power generating systems. A future closed cycle nuclear energy strategy has the advantage of harnessing additional energy from the reusable fissile and fertile fraction of used nuclear fuel by recycling it.

The prevalent method for recycling used nuclear fuel is to separate uranium and plutonium from used fuel that has been

dissolved in concentrated nitric acid using the Plutonium URanium EXtraction (PUREX) process and using the separated uranium and plutonium to fabricate new fuel. Currently international R&D for future recycling strategies involves optimising processes for separating long-lived minor actinide nuclides from spent or used nuclear fuel or from PUREX or other waste streams and transmuting or splitting them in specially designed reactors into fission products with shorter half-lives. This separation and fission or so-called partitioning and transmutation (P&T) strategy has obvious benefits for geological disposal of spent nuclear waste; it reduces the time for stewardship of the repository and the volume of repository space needed.

One of the greatest challenges of P&T is separating minor actinides from the chemically similar lanthanide fission products. These must be separated, as the lanthanides have high neutron cross sections and would drastically reduce the efficiency of transmuting the actinide nuclides. A number of processes for liquid-liquid extraction using selective ligands and auxiliary (or 'synergist') agents have been proposed[e.g. 3,4,5]. The nitrogen donor ligand 2,6-bis(5,6-dialkyl-1,2,4-triazin-3-yl)-pyridine (BTP) can selectively extract trivalent actinides (An(III)) over Ln(III) directly from nitric acid solution used in the dissolution of spent fuel[6]. XAS investigations for establishing the reason for this ligand's selectivity is summarised below.

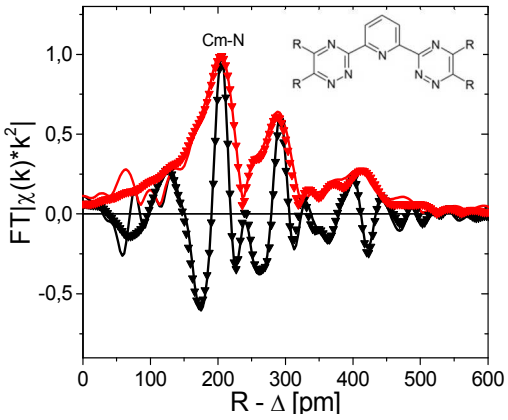

Figure 1. Fourier transform (FT) k^2-weighted Cm L3 edge EXAFS data for $[Cm(nPr\text{-}BTP)_3]^{3+}$. The first Cm-N coordination shell distance, uncorrected for phase shift Δ, is indicated. The molecular structure of BTP is shown as an inset.

The results of metal-nitrogen bond distances obtained from comparative An/Ln L3-edge extended X-ray absorption fine structure (EXAFS) studies of the coordination structure of 1:3 An(III) and Ln(III) cations (An = U, Np, Pu, Am, Cm; Ln = Nd–Lu) complexed with BTP performed over the last decade[7, 8] (an example for Cm L3 Fourier transform EXAFS data for $[Cm(nPr\text{-}BTP)_3]^{3+}$ is shown in Fig. 1) are depicted graphically in Fig. 2. The trend in bond length between Ln(III) and N atoms of the coordinating ligands going across the lanthanide series from Sm to Lu generally follows the known lanthanide contraction, being longest for Sm(III) and shortest for (Lu(III). In contrast, $[An(BTP)_3]^{3+}$ exhibits a near invariance of An(III)–N bond length with ionic radius (Fig. 2 bottom). These trends of trivalent metal-N distance as a function of ionic radius are reproduced by quantum chemical calculations, where the 5f electrons were treated explicitly[9]. We consider a strong

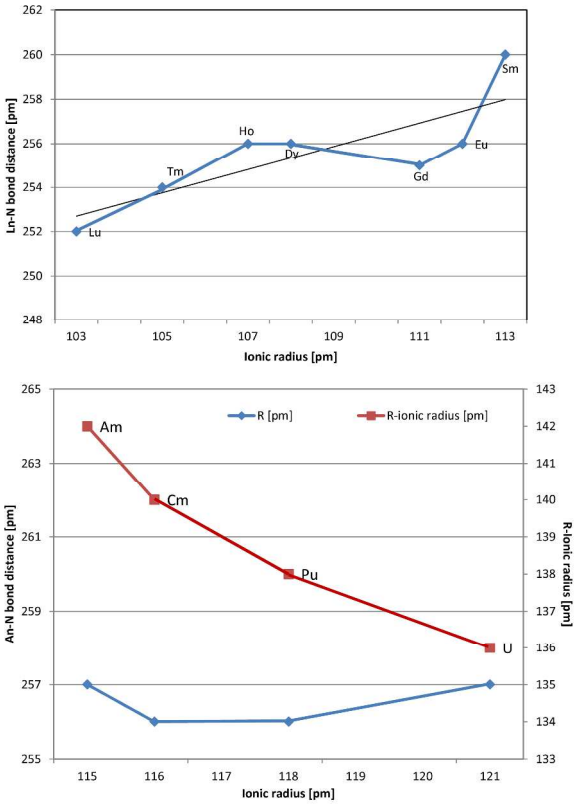

Fig 2. Ln-N (top) and An-N bond distances in $[M(BTP)_3]^{3+}$ solution complexes. The line in the Ln-N distance versus ionic radius is a linear fit to the data. An-N distances are compared to the difference between An-N (R) and the An(III) ionic radius (R-ionic radius).

deviation of the difference between metal-N distance (R) and the metal cation radius (R-Ionic radius) from a constant value, to be a measure of bond covalence; an ionic bond would be the sum of the ionic radii of the bonding partners. As the trend of Ln(III)-N primary coordination bond versus ionic radius follows the lanthanide contraction, we conclude this to indicate an ionic nature of Ln(III)-N bonding. Interestingly analysis of results also indicates that the nitrogen radius is 149-150 pm. In addition to plotting R as a function of ionic radius, the dependence of R-Ionic radius on metal cation radius for the An(III) complexes is shown in Fig. 2. The values range from 136 pm for $[U(nPr\text{-}BTP)_3]^{3+}$ to 142 pm for $[Am(nPr\text{-}BTP)_3]^{3+}$. The slope of the trend for the dependence of R on ionic radius is about zero, but the dependence of R-Ionic radius on ionic radius is nearly linear and the nitrogen radius in this case is determined to be much smaller, 142 pm, than for the Ln(III) series. We interpret this as indicating that the covalent character of the An(III)-N bond in these complexes is relatively greater compared to Ln(III)-N bonds in these complexes.

This interpretation is supported from $^{1}H,^{15}N$-HMQC NMR investigations, which provide direct evidence for higher

covalency in $[Am(nPr\text{-}BTP)_3]^{3+}$ compared to their analogous Ln(III) complexes[10]. Time-resolved laser fluorescence spectroscopy (TRLFS) results of 1:3 Cm(III) and Eu(III) BTP-complexes reveal that the increased covalency of the metal cation-ligand interaction is also associated with a greater thermodynamic stability of the $[Cm(nPr\text{-}BTP)_3]^{3+}$ complex.

Retention of neptunium in granite host rock

International consensus for the safe management of high-level long-lived nuclear wastes is via disposal in specially designed repositories, often referred to as Geological Disposal Fa-cilities (GDFs), located in deep geological formations far from the surface. The radiological toxicity of spent fuel and waste from reprocessing remains high up to hundreds of thousands of years so the long-term safety of GDF design generally relies on a multi-barrier system to isolate radioactive wastes from the biosphere. The multi-barrier system of a GDF consists of repository host rock (granite, clay, salt), the surrounding subsurface geo-environment, the engineered barrier system (EBS). The waste form, waste canisters, buffer materials, backfill, seals and plugs comprise the EBS. Each barrier hinders water intrusion and retards radionuclide release should water breach the repository. Prediction of the effectiveness of a GDF in isolating the radionuclides in the waste from the biosphere over a near geologic time domain is a formidable challenge. To reduce uncertainties associated with such predictions, experimental studies of the behaviour of components of the multi-barrier system are necessary[11].

In the following, results of a study of the distribution of actinide elements in a granite bore core originating from the underground rock laboratory in Äspö, Sweden,[12] that was used in a column tracer migration study, are summarised. Granite is considered a potential host rock for the disposal of radioactive wastes notably in the Nordic countries Sweden and Finland. The retention properties of pristine and altered granite are to this end of utmost importance.

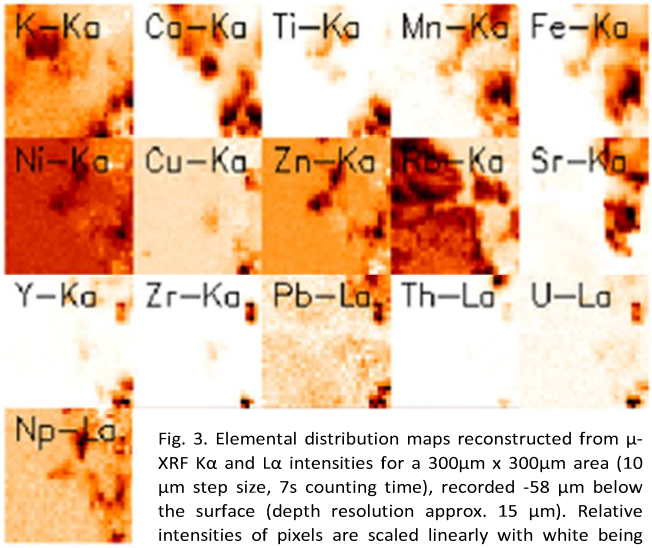

Fig. 3. Elemental distribution maps reconstructed from µ-XRF Kα and Lα intensities for a 300µm x 300µm area (10 µm step size, 7s counting time), recorded -58 µm below the surface (depth resolution approx. 15 µm). Relative intensities of pixels are scaled linearly with white being assigned the pixel with the smallest fluorescence intensity (0%) signal and black the pixel with the highest intensity (100%).

In the tracer experiment 14 mL of 10^{-5} mol/dm^3 237-Np(V) were introduced onto the granite bore core column and eluted with 80 mL ground water under pressure, whereby 26% of the Np introduced was recovered. Following the study, the bore core was cut into 4mm thick slices and analysed. The majority of the Np remaining on the column was found in the slice 30 mm from the column top (containing ~3 nmol Np/g; >1ppm)[13].

In order to ascertain the immobilisation mechanism for neptunium on the granite, initial scanning X-ray fluorescence experiments using a microfocussed beam (µ-XRF)[14] are performed on this slice. Measurements are performed in confocal geometry to probe sample volumes below the surface, which avoids potential artefacts from surface oxidation while at the same time minimizing spectral interference from other elements (in this case Np Lα1 and Sr Kα1 emission lines). Element distribution maps at different depths (e.g. in Fig. 3), reconstructed from this data, reveal the highest Np concentrations to be generally clustered in 1—3 pixels (pixel size of 20µm or 10µm), which are associated with small granite fissures ~100 µm or less in width. Analysis of Np L3 µ-XANES (Fig. 4) recorded at Np hot spots reveals that the Np(V) introduced onto the column is reduced to Np(IV) in the column. In addition, the elemental distribution maps show the Np distribution to be associated with Zn and Fe. Our initial conclusion is that ZnS or Fe associated with granite fracture material may have reduced Np(V) to less soluble Np(IV) and subsequent immobilization. Localisation of Np(IV) in small fissures may result from longer residence (i.e. reaction) times of inflowing Np in these smaller void spaces, compared to large fractures. Note that without the spatial resolution it would have been impossible to obtain this information at such a dilute tracer concentration.

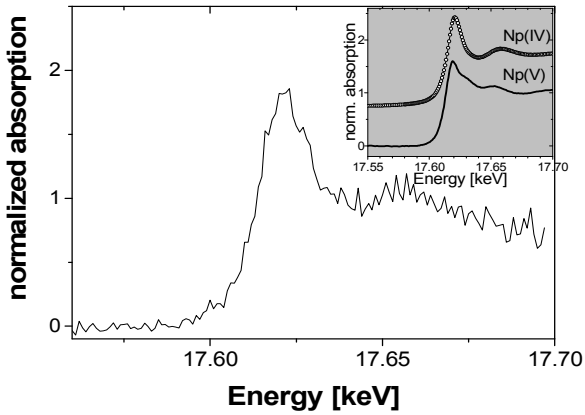

Fig. 4. Np L3 µ-XANES of a Np hot spot in the granite core slice studied. The inset shows reference spectra for comparison of Np(IV) and Np(V) (shifted along the y-axis for clarity).

Two interpretations for the observed clustering of high Np intensity pixels are plausible: 1) formation of a hydrolysed precipitate or 2) sorption of reduced Np(IV) species at localized areas on fissure walls. To determine which of these interpretations is correct, spatially resolved investigations with 125 nm resolution are performed[15]. A suitable section of the

granite slice is selected from low resolution µ-XRF maps, whereby a Np loaded fissure was localised and prepared using focussed ion beam (FIB; Zeiss NVision40 with a Ga liquid metal ion and field emission electron source; imaging with a GEMINI high resolution SEM) such that one of the fissure walls was exposed Fig. 5). A selection of two dimensional elemental distribution maps collected at the sample side with the exposed fissure wall is shown in Fig. 5, too. The K distribution shows the outline of the sample silhouette. These maps with higher spatial resolution reveal 100-400 nm Fe particles on the fissure wall. We did not find, however, any emission signal for Np in the sample. The Np was presumably lost when the fissure was exposed in preparation.

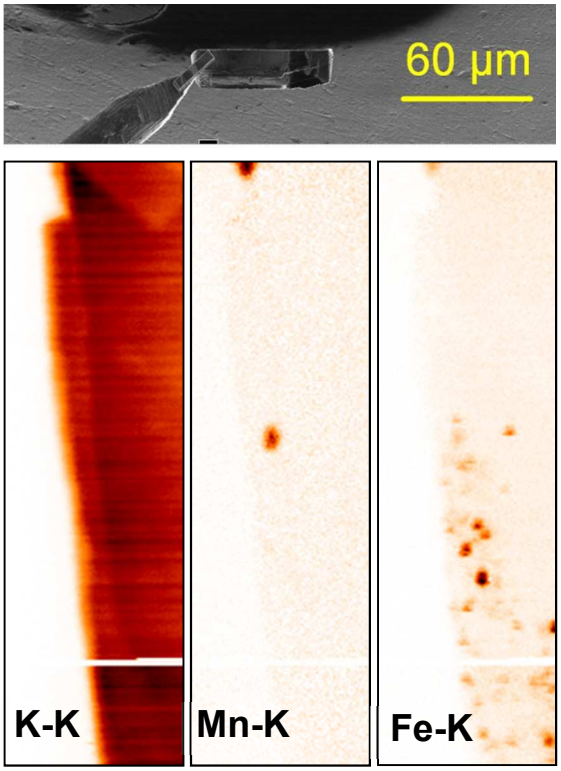

Fig. 5. Top: SEM micrograph of FIBed sample during lift-out. The pillar-shaped ~60 x 23 µm^2 sample is attached to a W tip micromanipulator with sputtered carbon, seen at the lower left. The lower right hand corner of the sample that appears rough is one of the sides of a fissure exposed during preparation. (Bottom) Element distributions for K, Mn and Fe (area=10.75 × 37.375 µm^2; 125 nm pixel size). The shadow in the K distribution at the top results from partial absorption of low energy K Kα emission from the sputtered carbon used as adhesive in sample mounting. The white lines in the images passing roughly through the middle of the exposed fissure wall are due to injection of the ESRF storage ring, where the measurements were automatically continued although no beam was present.

Addressing again our original question if the observed Np(IV) hot spots immobilized in the granite during the tracer study are present as precipitated hydrolysis particulate products or if they are present as sorbed Np localized at regions on the fissure walls, we conclude that Np(IV) is immobilised as hydrolysis particles. This is because no Np was observed in the nano-XRF maps of a fissure which originally exhibited Np fluorescence in the lower resolution µ-XRF screening studies prior to FIB preparation. As only nano-sized Fe structures were observed on the fissure wall, but no Np, and as it is unlikely that the Np was exclusively sorbed onto only one side of the fissure wall, we can safely conclude that Np was unlikely present as a sorbed species but likely present as particulate hydrolysis products formed when the Np(V) of the tracer solution was reduced to Np(IV). The Np(IV) formed subsequently hydrolysed to particles large enough to be occluded within the fissure. The Fe nanoparticulate structures on the fissure wall might have been involved in the reduction process responsible for Np immobilization.

Granite generally contains varying natural amounts of uranium and thorium and this natural background poses a potential source of contamination, should these elements dissolve and enter ground water upon drilling and excavation of shafts and deposition tunnels in the granite host rock for a nuclear waste repository. We therefore also characterised a number os small pieces of the granite slice for the U and Th distributions following the tracer experiment using nano-XRF tomography, absorption contrast tomography and phase-contrast tomography[15].

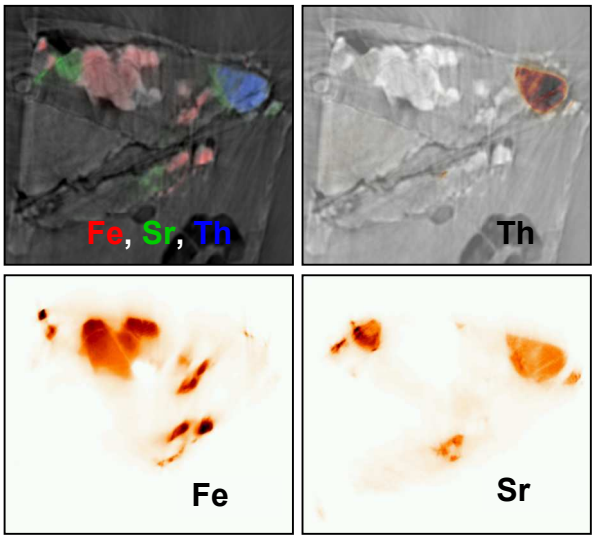

Fig. 6. Th, Fe and Sr distributions in a selected 215 x 193 µm^2 cross section of the granite slice studied reconstructed from nano-XRF tomographic sinograms. In the top row (left) a full-field tomographic cross section with Fe, Sr, Th as a red-green-blue overlay printed on top is shown, while (right) the tomographic cross section after phase-retrieval is shown with the Th distribution only. All images are scaled to 80% maximum intensity.

The reconstructed cross-section distributions for Th, Fe, Sr and Ca are shown in Fig. 6, along with an overlay of the distributions and the reconstructed in-line and X-ray phase contrast tomographic cross section of the sample section studied. The Th is concentrated in an approximate 35 µm wide, well-defined area in the upper quadrant of the images and exhibits fine fissures running through it with dimensions of a few micrometers. The Th distribution is positively correlated to the emission tomogram for Sr Kα fluorescence and with higher density areas (lighter grey scale in the phase contrast tomogram). As the Th distribution is not associated with that for Fe, we assume Th is likely not associated with biotite (or

associated altered phases such as clinochlore). If the observed fissures are considered an indication of cleavage planes at different angles, then this Th containing part of the granite rock might be a tectosilicate. As it is not apparently associated with either K or Ca (not shown), this Th containing grain may be a plagioclase feldspar comprised of majority sodium endmember, albite (Na K emission at ~1.05 keV is energetically too low to be observed here).

In contrast, in the areas investigated, we find the U distribution to be co-located with pores in the granite. However, where the pores are associated with hot spots of Fe, we find no U (not shown). Note that the tracer cocktail used contained no added thorium or uranium.

These results from combined CT tomographic and emission tomography studies reveal that the natural U and Th in the granite is associated with micro-pores and intimately associated with mineral phases, respectively. This suggests that the Th, as a structural component in a mineral and redox stable, is less likely than U, present in granite pores, to become mobile in groundwater upon drilling activities in the granite bed rock to construct a nuclear waste repository.

Determination of redox state using XANES and HR-XANES

As we have seen in the last section, the oxidation state of 5f-elements plays a determinant role in the balance between mobilisation and immobilisation processes and, hence, affects these elements' fate in the geosphere. One excellent method for determining redox states is via XANES investigation. XANES offers a number of advantages: it is applicable at relatively low concentrations and can be performed in situ, which allows studies of elements embedded as minority species in a majority matrix; the Np speciation in granite study summarised above being an example. XANES oxidation state determinations are also generally non-destructive, element-specific and sensitive.

Recent trends in such studies utilise energy dispersive analysing crystals to detect X-ray emission coming from the analyte with high energy resolution[see e.g. 16,17]. The resulting high resolution XANES (HR-XANES) or related techniques (such as resonant inelastic X-ray scattering) are being increasingly applied in actinide studies[1]. In the following, one example for characterisation of uranium in its hexavalent redox state, as the linear dioxo $(O=U=O)^{2+}$ uranyl cation, using U L3- and M4 HR-XANES are briefly summarised.

As the An elements, especially Pu, frequently occur in various oxidation states in the same system, determination of An valence is often challenging[18-20]. Because XANES involves photoelectron excitations about the ionisation energy, the valence state of an absorbing atom can be determined from the energy position of the XANES transition involved. In addition, XANES features are often a fingerprint of a particular species, so that comparison of observed features in unknowns with that for known compounds is often used for valence state determinations. This approach is, however, not always straightforward, particularly in valence mixtures. It is particularly difficult to differentiate between Np(IV) and Np(V), as their L3,2 absorption edges are only separated by ~2 eV and the energy position of Np(IV) appears above that for Np(V), which is in reverse order of the generally expected increase in ionization energy with increasing valence[20]. Using L3,2 edge EXAFS signatures of the short axial oxygen atoms (Oax) to quantify such mixtures can be used as a crutch a solution[21]. Determination of valence at the L3 edge energies of the actinide elements is also hampered by intrinsically low spectral energy resolution, due to the high angles of monochromator crystals necessary for experiments at these relatively short X-ray wavelengths, combined with the short lifetime of the excited core state.

One solution to overcome such difficulties is by using HR-XANES. An example of HR-XANES at both U L3[22] and U M4[23] edges for U(VI) in $Cs_2U^{VI}O_2Cl_4$ is shown in Fig. 7[24], whereby the two L3 HR-XANES depicted are recorded at two different angles of the linear uranyl units in a single $Cs_2UO_2Cl_4$ crystal relative to the incident photon beam polarization vector.

A well-known distinguishing feature in the conventional U L3,2 XANES of linear 'yl' cations is the multiple scattering (MS) resonance feature positioned around 10-15 eV above the main absorption maximum, or white line (WL). This feature results from scattering along the Oax atoms; its actual energy position depends on the An-Oax bond distance[25]. The better energy resolution in the HR-XANES is visibly evident in the clear separation of this MS feature from the WL. The polarisation dependence of this feature's intensity, being largest for a parallel orientation between the uranyl moieties and the polarisation (electric field) vector and nearly absent in the perpendicular orientation, supports its MS origin[cf 26]. In addition, a pre-edge at the onset of the rising absorption edge around 7 eV below the WL is revealed in the HR-XANES. This feature is due to partially allowed quadrupole transitions to 5f-like final states and is easily discernible in U(VI) spectra, with no f-electrons (higher transition probability), but less so (if at all) in U(V) or U(IV) HR-XANES. Therefore, it has been suggested that one can use this feature for An oxidation state determination in a manner similar to the extensively used 1s→nd quadrupole transitions in K-edge XANES investigations of transition metals.[27]

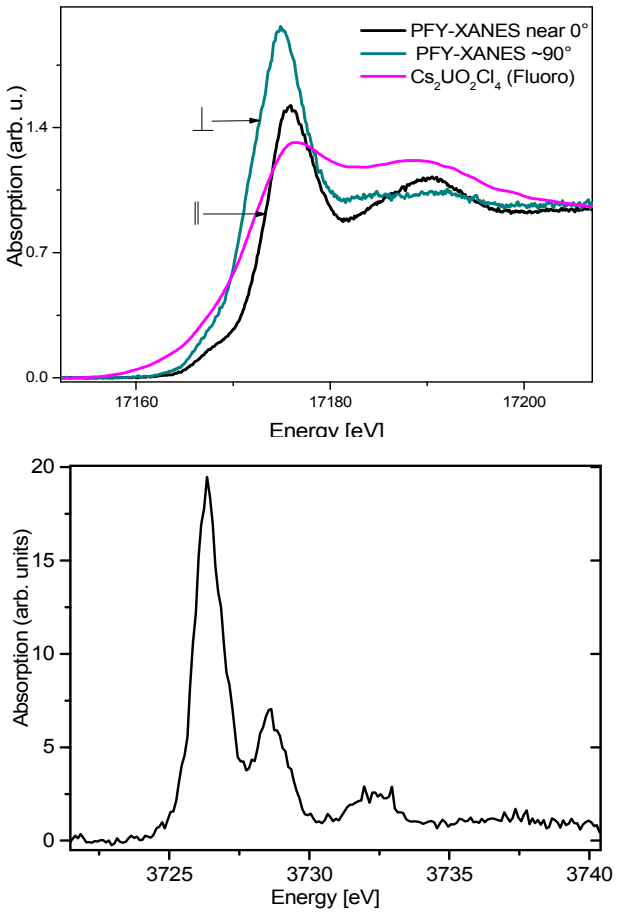

Fig. 7. (Top) U L3-edge HR-XANES recorded at two different angles of the linear $(O=U=O)^{2+}$ uranyl units in a single $Cs_2UO_2Cl_4$ crystal relative to the incident photon beam polarization vector, compared to a conventional XANES measured at near parallel orientation. (Bottom) U M4-edge HR-XANES of the same $Cs_2UO_2Cl_4$ crystal measured at an angle approaching 90°.

The fingerprint of the M4 HR-XANES can also be used to identify uranium oxidation state. The U M_4-edge involves $3d_{3/2} \rightarrow 5f$ electronic transitions and probe unoccupied orbitals with predominant U $5f$ character. The longer core-hole life-time and associated reduced broadening at the M4 edge leads to more sharpens spectral features than the L3 edge spectra. Note that these features are either not resolved in conventional spectra or reduced to a shoulder[28]. The fingerprint of the M4 spectrum in Fig. 7 is typical for uranyl[29] and only the main absorption peak at 3726 eV exhibits any polarisation dependence, but only in intensity and not energy position[24]. Furthermore, the M4 XANES for U(VI) compounds is reported to be relatively invariant to bond length[23]. This constancy makes its signature an excellent indicator for U(VI).

Note that this discussion is limited to the use of HR-XANES for characterisation of hexavalent uranium. The spectral features also contain information of electronic structure. A theoretical treatise of the spectral features of the specta in Fig. 7 is found in in ref. [24]. HR-XANES is not only an excellent means for oxidation state determinations in, e.g. mixtures[29]; due to the improved energy resolution, combined with and driving advances in our theoretical understanding of spectral features, HR-XANES and related techniques are providing insight into structure and bonding relationships by providing direct measures of occupancies and energies of frontier electrons. For example, analysis of the pre-edge structure in U L3 edge HR-XANES can emerge as extremely valuable for quantification of the degree of 5f orbital participation in U-O bonding.

Conclusions

In the first application example presented, one of the strengths of EXAFS is demonstrated: capability of obtaining structural information of systems without long-range order, in this specific case of solution samples. In addition, interpretation of the spectroscopic data underpins the molecular basis of separation processes. To summarize the results, we conclude that systematic EXAFS investigations, combined with other spectroscopies and theoretical quantum chemical calculations, provide evidence for a covalent character of the An(III)-BTP interaction, whereas the Ln(III)-N bonding is more ionic in character. This should allow improvement of complexant ligand design used in separations. Our experience also prompts proposing use of TRLFS as an facile means for screening or evaluating potential ligand performance through quantification of complex formation constants via comparative speciation investigations of the metal cations (Cm(III) or Am(III) versus Eu(III)) and candidate ligands. Development of ligands with improved specificity can present opportunities for new applications, such as in ion specific electrodes, selective membranes for smart linings or decontaminant foils or paints.

In the second example, results revealed that Np(V) immobilisation in granite from Äspö occurred via reduction to Np(IV), with Fe nanoparticulates decorating fissure walls possibly acting as the reductant. The Np(IV) is not retained in the granite due to subsequent sorption of the high valent, 'sticky' cations onto the fissure wall, but rather the Np(IV) formed subsequently hydrolyses to particles large enough to be occluded within the fissure. This has implications for modelling actinide retention in a granite host rock nuclear repository. The redox conditions of the groundwater/granite obviously play an important role, but realistic models must couple this to variations in hydrological transport affected by the size, composition and interconnectivity of granite fractures and fissures. This investigation and the tomographic studies of natural U and Th distributions and speciation in the granite are a preview of imaging tools available, which can be applied to investigations of specific sites selected for nuclear waste disposal to establish process understanding of mobilisation/immobilisation processes.

The utility of L and M edge HR-XANES for characterisation of hexavalent uranium was shown in the last example presented. HR-XANES and related high energy resolution X-ray techniques also provide information of electronic structure, which can serve to direct improvements in quantum chemical

descriptions of the heavy, relativistic actinide elements, certainly a non-trivial endeavour. With improved theoretical tools, benchmarked against experimental data, we should better be able to predict radionuclide behaviour, especially of the long-lived, 'problematic', alpha-emitting transuranic elements, essential for developing or improving nuclear fuels, reactor components, separations schemes, and potentially impact other areas such as radionuclides used as diagnostics or alpha-therapy in medical applications.

Acknowlegements

ANKA, APS, the ESRF and HASYLAB are acknowledged for awarding beamtime.

Notes and references

[a] The University of Manchester, Dalton Nuclear Institute, Pariser Building Floor G, M13 9PL Manchester, United Kingdom

1 M. Denecke, 'X-Ray Spectroscopy in Studies of the Nuclear Fuel Cycle', in *X-Ray Absorption and X-Ray Emission Spectroscopy: Theory and Application*, ed. by J. A. v. Bokhoven and C. Lamberti (Wiley, in print).
2 U. S. E. I. Administration, 'International Energy Outlook 2013', ed. by J. Conti and e. al (2013).
3 M. Nilsson, and K. L. N. Nash, *Solvent Extrraction and Ion Exchange,* 2007, **25**, 665−701.
4 S. Bourg, C. Hill, C. Caravaca, C. Rhodes, C. Ekberg, R. Taylor, A. Geist, G. Modolo, L. Cassayre, R. Malmbeck, M. Harrison, G. de Angelis, A. Espartero, S. Bouvet, and N. Ouvrier, *Nuclear Engineering and Design,* 2011, **241**, 3427-35.
5 G. Modolo, A. Wilden, P. Kaufholz, D. Bosbach, and A. Geist, *Progress in Nuclear Energy,* 2014, **72**, 107-14.
6 P. J. Panak, and A. Geist, *Chemical reviews,* 2013, **113**, 1199-236.
7 M. A. Denecke, A. Rossberg, P. J. Panak, M. Weigl, B. Schimmelpfennig, and A. Geist, *Inorganic Chemistry,* 2005, **44**, 8418-25.
8 N. L. Banik, M. A. Denecke, A. Geist, G. Modolo, P. J. Panak, and J. Rothe, *Inorganic Chemistry Communications,* 2013, **29**, 172-74.
9 N. L. Banik, B. Schimmelpfennig, C. M. Marquardt, B. Brendebach, A. Geist, and M. A. Denecke, *Dalton Transactions,* 2010, **39**, 5117-22.
10 C. Adam, P. Kaden, B. B. Beele, U. Mullich, S. Trumm, A. Geist, P. J. Panak, and M. A. Denecke, *Dalton Transactions,* 2013, **42**, 14068-74.
11 M. I. Ojovan, 'Handbook of Advanced Radioactive Waste Conditioning Technologies', (Woodhead Publishing).
12 I. Blechschmidt, and S. Vomvoris, '4 - Underground Research Facilities and Rock Laboratories for the Development of Geological Disposal Concepts and Repository Systems', in *Geological Repository Systems for Safe Disposal of Spent Nuclear Fuels and Radioactive Waste*, ed. by J. Ahn and M. J. Apted (Woodhead Publishing, 2010), pp. 82-118.
13 B. Kienzler, P. Vejmelka, J. Römer, and M. Jansson, *Nucl. Technol.,* 2009, **165**, 223-40.
14 M. A. Denecke, B. Brendebach, W. De Nolf, G. Falkenberg, K. Janssens, and R. Simon, *Spectrochimica Acta Part B: Atomic Spectroscopy,* 2009, **64**, 791-95.
15 M. A. Denecke, W. D. Nolf, A. Rack, R. Tucoulou, T. Vitova, G. Falkenberg, S. Abolhassani, P. Cloetens, and B. Kienzler1, 'Speciation of Actinides in Granite Subjected to Tracer Studies', in *Actinide Nanoparticle Research*, ed. by S. N. Kalmykov and M. A. Denecke (Heidelberg: Springer Verlag, 2011).
16 K. Hamalainen, D. Siddons, J. Hastings, and L. Berman, *Phys. Rev. Lett.,* 1991, **67**, 2850.
17 H. Hayashi, *Analytical Sciences,* 2008, **24**, 15-23.
18 K. Dardenne, A. Seibert, M. A. Denecke, and C. M. Marquardt, *Radiochimica Acta,* 2009, **97**, 91-97.
19 X. Gaona, J. Tits, K. Dardenne, X. Liu, J. Rothe, M. A. Denecke, E. Wieland, and M. Altmaier, *Radiochimica Acta,* 2012, **100**, 759-70.
20 M. A. Denecke, *Coordination Chemistry Reviews,* 2006, **250**, 730-54.
21 M. A. Denecke, K. Dardenne, and C. M. Marquardt, *Talanta,* 2005, **65**, 1008-14.
22 M. A. Denecke, M. Borchert, R. G. Denning, W. de Nolf, G. Falkenberg, S. Hönig, M. Klinkenberg, K. Kvashnina, S. Neumeier, J. Patommel, T. Petersmann, T. Pruessmann, S. Ritter, C. G. Schroer, S. Stephan, J. Villanova, T. Vitova, and G. Wellenreuther, *MRS Proceedings,* 2012, **1444**, mrss12-1444-y01-05.
23 T. Vitova, M. A. Denecke, J. Göttlicher, K. Jorissen, J. J. Kas, K. Kvashnina, T. Prüßmann, J. J. Rehr, and J. Rothe, *Journal of Physics: Conference Series* 2013, **430**.
24 T. Vitova, J. C. Green, R. J. Denning, M. Löble, K. Kvashnina, J. J. Kas, J. J. Rehr, T. Malcherek, and M. A. Denecke *(*in prep).
25 M. A. Denecke, in *Workshop on Speciation, Techniques and Facilities for Radioactive Materials at Synchrotron Light Sources*, ed. by T. Riech (Grenoble: OECD-NEA, 1998), p. 135.
26 E. A. Hudson, P. G. Allen, L. J. Terminello, M. A. Denecke, and T. Reich, *Physical Review B,* 1996, **54**, 156-65.
27 T. Vitova, K. O. Kvashnina, G. Nocton, G. Sukharina, M. A. Denecke, S. M. Butorin, M. Mazzanti, R. Caciuffo, A. Soldatov, T. Behrends, and H. Geckeis, *Physical Review B,* 2010, **82**, 235118.
28 J. Petiau, G. Calas, D. Petitmaire, A. Bianconi, M. Benfatto, and A. Marcelli, *Physical Review B,* 1986, **34**, 7350-61.
29 K. O. Kvashnina, S. M. Butorin, P. Martin, and P. Glatzel, *Physical Review Letters,* 2013, **111**.

A summary of innovative techniques using synchrotron radiation for actinide studies in nuclear research, including X-ray spectroscopy and imaging.